NANO LETTERS

Letter

pubs.acs.org/NanoLett

Nonlinear Photon-Assisted Tunneling Transport in Optical Gap Antennas

Arnaud Stolz,[†] Johann Berthelot,[†] Marie-Maxime Mennemanteuil,[†] Gérard Colas des Francs,[†] Laurent Markey,[†] Vincent Meunier,[‡] and Alexandre Bouhelier*[,†]

[†]Laboratoire Interdisciplinaire Carnot de Bourgogne CNRS-UMR 6303, Université de Bourgogne, 21078 Dijon, France

[‡]Department of Physics, Applied Physics, and Astronomy, Rensselaer Polytechnic Institute 110 Eighth Street, Troy, New York 12180-3590, United States

ABSTRACT: We introduce strongly coupled optical gap antennas to interface optical radiation with current-carrying electrons at the nanoscale. The transducer relies on the nonlinear optical and electrical properties of an optical gap antenna operating in the tunneling regime. We discuss the underlying physical mechanisms controlling the conversion involving d-band electrons and demonstrate that a simple two-wire optical antenna can provide advanced optoelectronic functionalities beyond tailoring the electromagnetic response of a single emitter. Interfacing an electronic command layer with a nanoscale optical device may thus be facilitated by the optical rectennas discussed here.

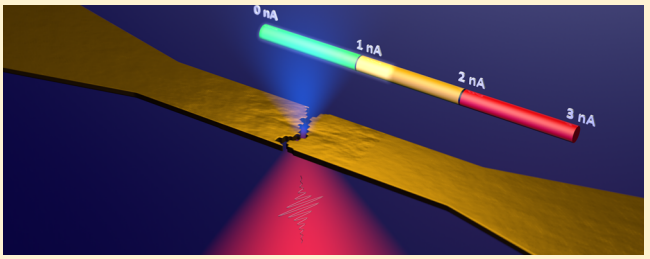

KEYWORDS: *Plasmonics, photon-assisted tunneling, optical rectennas, electromigration*

Giant enhancement of optical fields are generally locally produced in the feedgap formed between two or several adjacent resonant metal nanoantennas.[1,2] Strongly coupled optical antennas are thus essential for amplifying weak optical interaction cross sections such as the vibrational responses of a single molecule[3,4] or nonlinear $\chi^{(2)}$ and $\chi^{(3)}$ processes.[5−8] When the separation distance between the individual constituents of the optical antenna reduces, large Coulomb splitting of the underlying plasmonic modes takes place.[9−11] For an atomic-scale gap, charge transfer plasmons are driving the antenna response in the so-called quantum tunneling regime.[12−15] In this case, the quantum nature of the interaction opens a new paradigm for utilizing optical gap antennas beyond the control of electromagnetic fields at the nanometer length scale.[16,17] For instance, incoming photons can exchange energy with tunneling charges modifying thus the conductance of the barrier[18,19] and strong-field effects were recently reported.[20,21] Therefore, adopting metal-based optical gap antennas as a disruptive technological vehicle may provide advanced functional devices to interface nanoscale electronics and photonics. Several steps were recently made in this direction by electrically wiring optical feedgaps where an enhanced optical field is self-aligned with large static electric fields (10^7−10^9 V/m).[8,22,23]

Inspired by these advances, we demonstrate here that ultrafast laser pulses can interact with tunneling charges in an electrically wired optical feedgap. The geometry discussed here transduces the laser field through a photon-assisted tunneling mechanism to create a nanometer-scale nonlinear rectifying antenna, or rectenna, operating at optical frequencies. We show that the rectenna's nonlinear transducing yield is driven by the electrical environment of the feedgap. Specifically, the crossover between a linear intensity dependence of the photocurrent and a multiorder power law is strongly reduced at the onset of Fowler−Nordheim tunneling.

Photon-Assisted Tunneling. Following the description by Tucker,[24] the time-averaged photon-assisted tunneling current of a junction subject to an electromagnetic field is[22,25,26]

$$\langle I_b \rangle = \sum_{n=-\infty}^{\infty} J_n^2\left(\frac{eV_{opt}}{\hbar\omega}\right) I_b\left(V_b + \frac{n\hbar\omega}{e}\right) \tag{1}$$

where V_{opt} is the voltage drop at the junction, J_n is an nth order Bessel function, ω is the angular frequency of the radiation, e is the elementary charge, and V_b is a static bias applied to the junction. Retaining the lowest order terms $n = 0$ and $n = \pm 1$ and using the asymptotic forms of the J_n, the tunneling current writes as a sum of a static tunneling contribution and a photon-assisted term

$$\langle I_b \rangle = I_b(V_b, V_{opt} = 0) + \frac{1}{4}V_{opt}^2\left(\frac{I_b\left(V_b + \frac{\hbar\omega}{e}\right) - 2I_b(V_b) + I_b\left(V_b - \frac{\hbar\omega}{e}\right)}{\left(\frac{\hbar\omega}{e}\right)^2}\right) \tag{2}$$

For junctions consisting of Au electrodes, the energy dispersion of the tunneling transmission near the Fermi level

Received: December 19, 2013
Revised: March 14, 2014
Published: April 3, 2014

   dx.doi.org/10.1021/nl404707t | *Nano Lett.* 2014, 14, 2330−2338

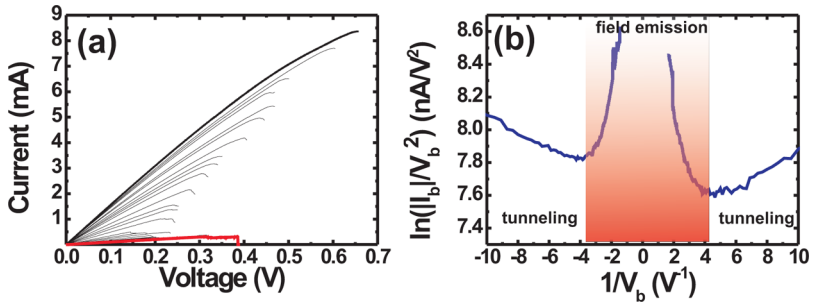

Figure 1. (a) Current−voltage plot of a Au nanowire for a series of subsequent bias sweeps. For each sweep, the voltage ramp is manually stopped before electrical failure of the nanowire. The resistance increases between sweeps as the result of the formation of a constriction. Eventually, the process leads to the electrical failure of the nanowire (red curve). (b) Fowler−Nordheim representation of the electrical characteristic of an optical gap antenna produced by electromigration. The edges of the shaded area are the transition voltages indicating the type of transport.

ε_F is slowly varying around $\varepsilon_F \pm \hbar\omega$ if $\hbar\omega < 2$ eV.[27] Thus, the time-average tunneling current may be written in the classical form of rectification

$$\langle I_b \rangle = I_b(V_b, V_{opt} = 0) + \frac{1}{4} V_{opt}^2 \frac{\partial^2 I_b}{\partial V_b^2} = I_b + I_{phot} \quad (3)$$

Optical rectification is possible if the response time of the junction is fast enough for the electrons to tunnel through the barrier in half of a cycle of the external optical field.[25] A low junction capacitance is therefore a necessity that requires nanostructure-based devices.[22] In this respect, optically coupled antennas are especially appealing because of their nanometer-scale active feedgap area and the capability at concentrating and enhancing an incident electromagnetic field.

Electrical Characterization of Connected Optical Antennas. In this work, we produce nanometer-scale optical gap antennas by controlling the electromigration of 100 nm wide 5 μm long gold nanowires fabricated on a glass substrate.[28,29] The nanowires and their electrical connections are realized by a double-step lithography. Macroscopic electrodes and a series of alignment marks are first fabricated by standard optical lithography. The marks are used for subsequently defining nanowires by electron-beam lithography. A 2 nm thick layer of Cr followed by 50 nm of Au are then thermally evaporated to form the metal structures. A liftoff of the electron-sensitive resist finalizes the sample.

Figure 1a shows a typical current−voltage plot of a contacted nanowire when a ramping bias is applied to the terminals. At the onset of electromigration, the curve is departing from an Ohmic behavior.[30] The formation of a constriction preceding that of a nanometer-scale gap is controlled by applying successive bias sweeps that eventually lead to the electrical failure of the nanowire (red curve).[29] The breakdown is confirmed when the conductance of the gap G is smaller that the quantum of conductance $G_0 = 77.4$ μS. We find that approximately 60% of the junctions produced by this method lead to gap sizes commensurate with electron tunneling. The Folwer−Nordheim representation of Figure 1b illustrates the current response after electromigration. The tunneling current I_b is measured with a 10^8 V/A current-to-voltage converter. The minima in the curve at −3.8 and 4.2 V^{-1} indicate transition voltages consistent with previous voltage spectroscopy of atomic Au junctions.[29,31] These transition voltages were originally thought to determine the crossover between a direct-tunneling transport to a field emission regime.[32] The height ϕ of the potential barriers can be directly deduced from these two minima.[29,33] With this interpretation of the transition voltages, we measure $\phi^D = 0.23$ eV and $\phi^S = 0.26$ eV for the barriers at the drain (D) and source (S) electrodes, respectively. In a recent contribution by Wu and co-workers, transition voltages were however shown to depend on the atomic configuration of junction and the local density of states rather than the shape of the barrier.[34] While the interpretation of the transition voltage is still under debate, the process of electromigration typically produces a stochastic rearrangement of the Au leads and are thus inherently asymmetric.[8,35] Geometrical asymmetry of the gap, even constituted from the same material, can lead to different electrostatic potentials.[25,34,36] A slight asymmetry in the Fowler−Nordheim representation as in Figure 1b was systematically observed in our experiments. When measurable, transition voltages in all tested devices were consistently observed for $V_b < 0.6$ V.

Photoresponses of the Junction. We then interrogate the nonlinear photon-assisted tunneling transport of such contacted optical gap antenna by laterally scanning the structure through the focus of a tightly focused titanium:sapphire pulsed laser beam. A schematic of the setup is illustrated in Figure 2.

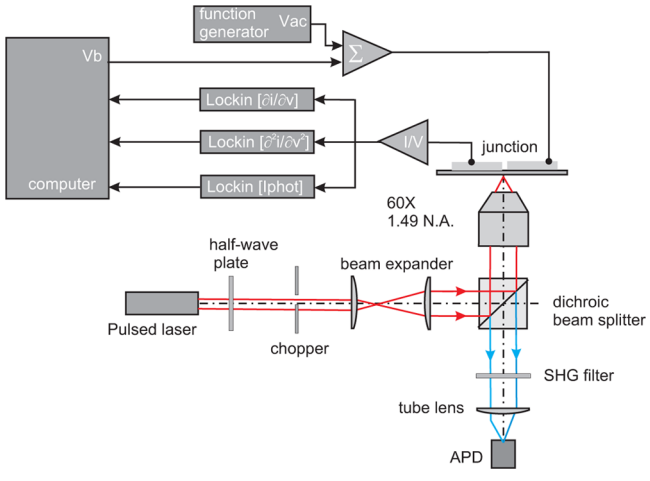

Figure 2. Sketch of the experimental setup. The junction is irradiated with a laser emitting 180 fs pulses with a repetition rate of 80 MHz centered at a wavelength of 810 nm. The filtered second harmonic response is detected by an avalanche photodiode. The influence of the laser on the tunneling transport is recorded by lockin amplifiers detecting the photocurrent synchronized at the chopping frequency of the laser, signals proportional to the differential conductance, and its nonlinearity.

dx.doi.org/10.1021/nl404707t | Nano Lett. 2014, 14, 2330−2338

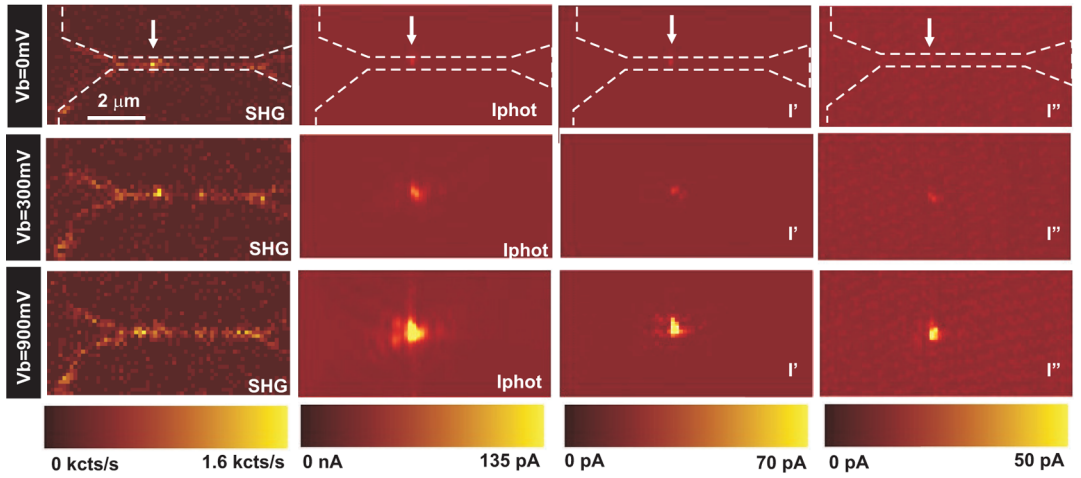

Figure 3. (x,y) spatial dependence of the second harmonic signal (first column on the left), the demodulated laser-induced current I_{phot} (second column), the signal provided by the differential conductance I' (third column), and the signal proportional to the nonlinear conductance I'' (last column) for three biases V_b = 0 mV, V_b = +300 mV, and V_b = +900 mV, respectively. The electrode and nanowire contours are represented by the dashed layout for V_b = 0 mV. The arrows show the spatial location of the antenna feedgap. The bias is applied to the left electrode.

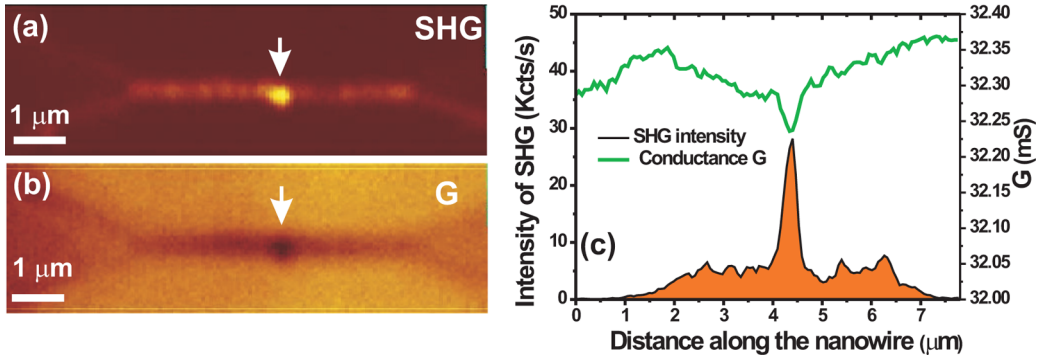

Figure 4. (a) SHG signal from a pristine Au nanowire (before electromigration). A defect at the nanowire surface gives rise to a large SHG response (arrow). (b) Simultaneously acquired conductance map. The conductance drop is maximum at the location of the defect. (c) Cross sections taken along the nanowire. The drop at the defect is about 0.14 mS.

The photon energy is fixed at 1.53 eV. The pulse duration at the exit of the laser and the repetition rate are 180 fs and 80 MHz, respectively. The numerical aperture (N. A.) of the focusing objective is 1.49. For each lateral (x,y) position of the antenna in the focus, we conduct photon-dependent inelastic tunneling spectroscopy by measuring the first and second derivatives of the current. To that purpose, a small modulated bias $V_{mod} = V_{ac} \cos(2\pi F_{mod} t)$ is added to the static voltage V_b applied to the nanojunction with V_{ac} = 15 mV and F_{mod} = 1 kHz. Two lock-in amplifiers referenced at F_{mod} and $2F_{mod}$ output a signal proportional to the differential conductance $I' = V_{ac}(\partial I_b/\partial V_b)$ of the gap antenna and signal proportional to the nonlinearity of the conductance $I'' = 1/4V_{ac}^2(\partial^2 I_b/\partial V_b^2)$, respectively. The laser-induced current I_{phot} is extracted by chopping the laser beam at F_{chp} = 400 Hz and by demodulating the tunneling current I_b at F_{chp} with a third lock-in amplifier. Finally, we also record the second-harmonic generated (SHG) from the gold structure by detecting the radiation emitted at 3.06 eV with a single-photon avalanche photodiode. The SHG signal was detected through a 124 meV wide bandpass filter centered at 3.06 eV. Because of the geometrical asymmetry of the feedgap and the electromagnetic build-up in the interstice,[1,2] the tunneling junction exhibits an enhanced SHG response[8] providing an imaging contrast to locate the antenna feedgap.

Figure 3 displays a series of (x,y) scans of the different gap responses under a constant average laser intensity at focal spot of 840 kW/cm^2. With the characteristics of our pulses, the instantaneous peak intensity at the focus is 58 GW/cm^2. The polarization of the laser is aligned along the nanowire for the remaining of the discussion and, when relevant, average intensities are indicated. The simultaneously measured SHG, photocurrent I_{phot}, the current proportional to the linear conductance I', and the current given by the nonlinear conductance I'' are displayed for a null bias in the top images. The dashed lines follow the contours of the structure. While the SHG signal is expectedly large at the Au edges, the strongest nonlinear response is observed at the position of the electromigrated gap[8] as indicated by the arrows. When the femtosecond-pulsed laser overlaps the feedgap, a 20 pA photocurrent is produced at F_{chp} in the absence of a static bias (V_b = 0 V). At the same position, electrical changes of the lockin outputs I' and I'' are measured.

From the concomitant occurrence of these signals at a very well-defined spot it is tempting to conclude that a photon-assisted tunneling process described by eq 3 is the dominating mechanism. Even with a small asymmetry of the barrier heights, a net rectified current flowing in the antenna feedgap can be generated owing to the nonlinear characteristics of the junction.[37] Thermal effects, however, can drastically influence

dx.doi.org/10.1021/nl404707t | Nano Lett. 2014, 14, 2330−2338

the conduction properties of a laser irradiated tunneling junction as reviewed by S. Grafström.[38] Among possible processes resulting from photon absorption in the metal and subsequent Joule heating, let us mention thermal expansion of the gold leads, thermally assisted tunneling resulting from an nonequilibrium electron distribution,[39] and thermovoltages arising from a temperature gradient between the two sides of the feedgap.[40]

Evaluation of Thermal Effects. In the following, we estimate the possible contribution of these effects to explain the photocurrent at zero bias observed in Figure 3. Thermal expansion was shown to be negligible in planar metal junctions lying on a substrate and illuminated under a constant-wave (CW) laser excitation.[22,41] For a pulsed excitation, the effect of a light-induced thermal expansion in the I_{phot} or I' maps of Figure 3 would be distributed along the nanowire and not be uniquely restricted to the antenna feedgap. Although, sharp discontinuities are known to increase electromagnetic confinement, the temperature rise at the edge of a Au nanowire was shown to remain modest (<10%) and is mostly accounted for a reduced heat dissipation and not due to an increased absorption cross-section.[42]

Nevertheless, to estimate the steady-state temperature resulting from the absorption of the pulses, we measure the photoinduced change of conductance $G_d - G_T$ at $V_b = 0$ V of an as-fabricated nanowire before electromigration. Here, G_d is the dark conductance measured without laser excitation and G_T is the conductance when the temperature is changed. Figure 4a,b shows the simultaneously acquired SHG and conductance maps for an unbroken nanowire laterally scanned through the laser focus. The laser intensity is here 1250 kW/cm^2, a value slightly higher than the one used in Figure 3. Generally, whenever the metal surface is overlapping the focal spot the conductance diminishes: the electrode and nanowire outlines are readily recognized by the darker contrast in Figure 4b. At the center of the nanowire there is a strong SHG response (arrow) indicative of the presence of a morphological defect formed during the fabrication. The strong SHG signal is accompanied by a reduction of the electrical conductance of the nanowire as shown in Figure 4b. The defect and/or its SHG activity act as an entry point for an increased laser absorption. However, despites this SHG-induced conductance change, $G_d - G_T$ remains modest at a value below 0.14 mS as shown by the cross-sectional cut along the nanowire displayed in Figure 4c.

We have calibrated the temperature dependence of the conductance by placing a substrate containing three nanowires on a temperature-controlled Pelletier element. Figure 5 shows a linear temperature dependence[43] for the three nanowires where $G_{amb} - G_T$ is the difference between the conductance measured at ambient temperature and the conductance measured when the Pelletier element is heated. Linear fits (dashed curves) through the data point lead to an average slope of 0.0147 mS/K. Considering the drop of conductance upon laser absorption shown in Figure 4 (<0.14 mS), the temperature rise is estimated at approximately 9 K. Heat is thus efficiently removed from the nanowire through the extended metal leads. This is confirmed by the lateral variation of the conductance along the nanowire. Because the terminals for the connected gaps are the essentially the same, we conclude that they act as efficient heat sinks and a laser-induced increase of the nanowire temperature is unlikely to explain the photocurrent in Figure 3 in accordance with the recent work of Herzog et al.[43]

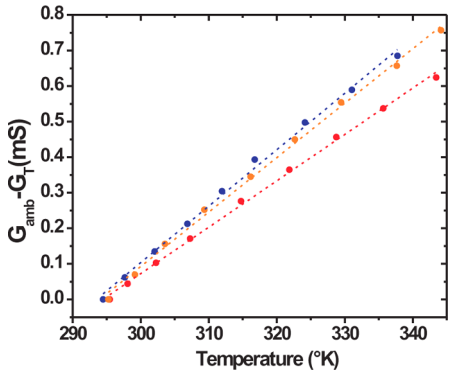

Figure 5. Temperature dependence of the conductance measured for three nanowires with similar dimensions. The variation is referenced to the conductance measured at ambient temperature G_{amb}. Linear fits through the data lead to a mean slope of 0.0147 mS/K.

Thermal processes are providing well-defined characteristics when the junction is scanned through the focus such as a sign reversal of the current.[40,44] Figure 6 shows an example of a thermo-current in an electromigrated junction. In this experiment, the laser intensity was intentionally kept large at 4 MW/cm^2. The confocal map of Figure 6a displays the spatial dependency of the second harmonic generation of the structure. At the location of the antenna feedgap near the left contact, the second harmonic activity is amplified.[8] The current map displayed in Figure 6b shows the magnitude of the photocurrent flowing through the junction for null bias. There is a clear contrast reversal of the current between the two sides of the feedgap. When one electrode is at a different temperature than the other, a thermovoltage builds up across the gap.[38] The sign of the thermovoltage changes with the position of the gap with respect to the laser focus.[40,44] When the latter is centered across the gap, the net current is zero as observed in Figure 6b. Note that we expect a similar change of contrast for a thermally assisted tunneling process. The influence of the laser absorption can be traced along the right part of the nanowire where the negative value of the current increases to reach its maximum at the right edge of the feedgap. Because the gap was produced near the left electrode, dissipation along the long arm is therefore reduced compared to the left side located closer to the macroscopic heat sink.

The experiment was repeated with a 10-fold reduction of laser intensity (416 kW/cm^2). Figure 6d shows the SHG and I_{phot} responses for another device. Under this excitation intensity, the photocurrent map is vastly different and we do not measure a change of contrast in the current distribution. The behavior of this junction is essentially similar to the one already observed in Figure 3. We consistently measured similar I_{phot} distributions at $V_b = 0$ mV with amplitudes varying from device to device.

To conclude this section, we observe that for modest average laser intensities, the elevation of temperature can be neglected (Figure 4), and because there is no evidence of current reversal the photocurrents generated in the antenna feedgap at $V_b = 0$ mV in Figures 3 and 6d are unlikely related to thermal effects.

Bias Dependence of the Photocurrent. Within the assumptions discussed by Mayer and co-workers[25] and by Ward et al.,[22] the classical picture of photon-assisted tunneling is dictated by eq 3. This relation indicates that rectified current I_{phot} is given by the magnitude of the optically induced voltage drop V_{opt} at the junction and the nonlinearity of the

dx.doi.org/10.1021/nl404707t | Nano Lett. 2014, 14, 2330−2338

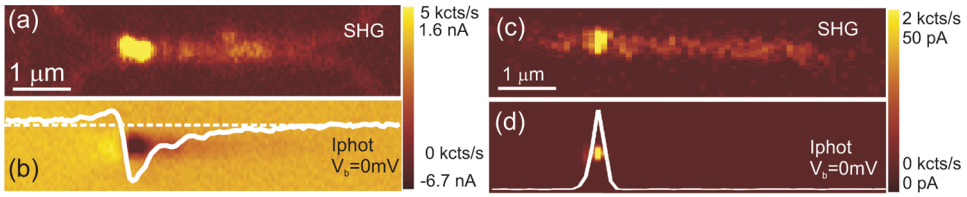

Figure 6. (a) Confocal map showing the second-harmonic signal enhanced at the rectenna feedgap. (b) Spatial distribution of the tunneling current for V_b = 0 mV. The laser intensity is 4 MW/cm^2. The contrast reversal across the antenna feedgap is typical from thermocurrents. (c,d) Confocal maps for a laser intensity of 416 kW/cm^2 and V_b = 0 mV. There is no evidence of a changing current sign. The same color scale is used for the SHG unit (kcts/s) and the photocurrent unit (nA).

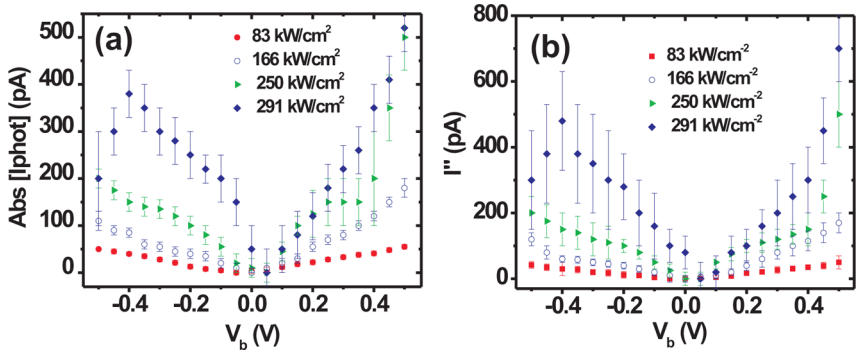

Figure 7. Bias dependence of the absolute value of the photocurrent (a) and (b) the current proportional to the nonlinearity of the antenna conductance for increasing laser intensity $I'' = 1/4V_{ac}^2(\partial^2 I_b/\partial V_b^2)$. $|I_{phot}|$ and I'' are correlated indicating that the rectification picture is the dominant mechanism for all the laser intensities and bias values investigated.

conductance $\partial^2 I_b/\partial V_b^2$. To verify that the optical gap antenna discussed here behave like a semiclassical rectenna, we operate the device of Figure 3 at different points of its electrical characteristics by applying a static voltage V_b across the feedgap. The spatial responses of the tunneling gap antenna for V_b = +300 mV and V_b = +900 mV are shown in the series of images in the middle and bottom parts of Figure 3. For this particular device and under these biases, electron transport in the rectenna is driven by direct-tunneling (no inversion point in the Fowler–Nordheim plot). The transmittance and therefore the differential conductance $\partial I_b/\partial V_b$ of the rectenna increases with bias. In this region of the current–voltage characteristic, the nonlinearity of the conductance $\partial^2 I_b/\partial V_b^2$ becomes larger as demonstrated in Figure 3.

The yield of optical rectification is generally driven by the classical responsivity S

$$S = \frac{\frac{\partial^2 I_b}{\partial V_b^2}}{\frac{\partial I_b}{\partial V_b}} \quad (4)$$

S strongly depends on the electrical nonlinearity of the barrier and can be increased by applying an external bias voltage V_b. For solar-harvesting applications, the electrical power provided by the application of a bias should remain smaller than the power gained by rectifying the external radiation.[25] However, for purposes where transducing optical gap antennas are used as optoelectronic interfacing devices, a bias-dependent responsivity may be desired to control the flow of information.

In Figure 3, the classical responsivity at the feedgap is S = 0.2 V^{-1} at zero bias and increases linearly with bias with a slope of ~0.3 V^{-2}. We measure a 6-fold enhancement of I_{phot} when V_b is increased from 0 to +900 mV. The simultaneously recorded SHG signal is stable within a few percent during the bias increments. Minor variations are attributed to a slight drift of the focus between successive scans. The relative stability of the harmonic response is a good indication that the structural integrity of the feedgap is maintained during the experiment. SHG is strongly affected by symmetry and local defects, and any significant modifications of the junction geometry or the leads would have been recorded in the SHG maps. Although SHG and I_{phot} are both proportional to V_{opt}^2, we could not identify a direct relationship between the SHG activity and the amplitude of the photocurrent for the fixed polarization state used in this work. The magnitude of the photocurrent strongly depends on the gap spacing and the SHG response on the underlying symmetry of the system[8] and local electromagnetic field distribution. Because the junctions formed by electromigration are notoriously irregular with various ranges of gap distances, it is difficult to extract a clear relationship between quantities that depend on different structural parameters.

Figure 7 shows the bias dependence of the photocurrent $|I_{phot}|$ and the lockin output I'' given by the nonlinearity of the conductance $1/4V_{ac}^2(\partial^2 I_b/\partial V_b^2)$. The curves were obtained from a device different that the junction discussed in Figure 3. The evolution of the photocurrent curves for all bias values and laser intensities are well reproduced by I''. The correlation between Figure 7 panels a and b strongly suggests that the photocurrent is driven by eq 3 and that the classical picture of photon-assisted tunneling (optical rectification) is at play.[22] The amplitudes of the $|I_{phot}|$ and I'' signals are occurring on the same current scale implying that the optically induced voltage drop V_{opt} is comparable to the modulation bias V_{ac}, in this case 15 mV. This value agrees well with the values inferred for a CW excitation with similar devices.[22] For large laser intensities and bias voltages, we observe an irreversible damage of the device as shown by the drop of the photocurrent for $V_b < -0.4$ V at 291 kW/cm^2.

dx.doi.org/10.1021/nl404707t | Nano Lett. 2014, 14, 2330–2338

Intensity Dependence of the Photocurrent. Figure 8 shows the evolution of the rectified current I_{phot} with the

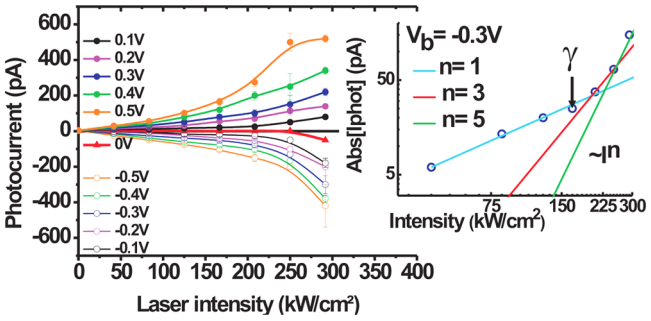

Figure 8. Dependence of the photocurrent I_{phot} on the average laser intensity for different symmetric biases V_b. Inset: Double-logarithmic plot of $|I_{phot}|$ versus average laser power for $V_b = -0.3$ V. For moderate pulsed laser intensities, the photocurrent scales linearly with intensity. Higher-order photon processes are occurring when the laser intensity is increased. γ denotes the transition from a linear regime to a power law dependence with $n > 2$.

average laser intensity for a series of negative and positive voltages V_b. The data were acquired from the device used in Figure 7. The laser intensity dictates the regime of operation of the optical rectenna. For moderate laser intensities and regardless of the applied bias, the rectenna operates in a linear regime. This low-excitation regime, discussed below, is consistent with the behavior reported for a discontinuous gold film[45] and for extended Ag−Al_2O_3−Al junctions.[46] An example of a linear relationship is shown in the double-logarithmic plot in the inset of Figure 8 for $V_b = -300$ mV. The data below ~200 kW/cm^2 (γ-point) are well fitted by a linear trend with a slope of 14 pA/kWcm^{-2}. At γ, we estimate that 2.5 × 10^3 photons are needed to produce an electron assuming a sensitive area of 1 nm × 100 nm. After the threshold γ, the trend is no longer linear; multiphoton processes triggered by the ultrafast laser pulses are contributing to the photocurrent as indicated by the increasing power-law exponent with laser intensity.

Role of d-Band Electrons. Multiphoton absorption leads to a photoemission for excitation energies above the barrier[47] or to tunneling of excited electrons in states located above the Fermi surface but remaining below the work function.[46] The electrical conductance in a nanoscale junction typically involves tunneling of electrons located near the Fermi level ε_F,[48] which for gold are located within the sp conduction band. Taking into account the mean reduced effective barrier height of the electrodes at feedgap [Figure 1b], a single photon absorption by an electron located near ε_F gains an excess energy of $\hbar\omega - \phi^{D,S} \sim 1$ eV above the effective barrier. Under this excitation energy, the photocurrents resulting from a one-photon or even a multiphoton above-threshold emission are well described assuming a static barrier[46,48,49] and should be independent of the classical responsivity S of the rectenna. This is in direct contrast with Figure 7 for the range of laser intensities used in this work.

Viljas and Cuevas calculated that the photoconductance between two Au atoms increases when d-band electrons are optically excited.[27] The importance of interband contribution in the hot carrier distribution was also recently pointed out by Govorov et al.[50,51] and was considered for explaining the nonlinearities in tip-enhanced photoemission.[52] Transition of upper-edge d electrons to ε_F occurs for optical energies as low as 1 eV[53,54] at the X-point of the Brillouin zone; direct interband transitions are thus possible with our laser energy.

To gain insight into the emission processes and how they relate to the band-structure of the gold electrodes, we now present an analysis based on the calculated band-structure of gold. To that end, we employed density functional theory (DFT) using exchange-correlation functional expressed within the general gradient approximation (GGA) of Perdew−Burke−Ernzerhof (PBE).[55] Our calculations include spin−orbit (SO) coupling corrections. The PBE+SO approach has been shown to yield band structures in excellent agreement with experiment.[54] In addition, scalar-relativistic DFT calculations have been used previously to successfully account for inter- and intraband transition in gold.[56] The calculations were performed using the DFT package VASP 5.2.12[57] with scalar-relativistic corrections, a projector augmented-wave (PAW) pseudopotential,[58] a 288 eV energy cutoff, and a dense k-point grid (1771 nonequivalent points) to sample the Brillouin zone. Decomposed density of states was computed using the tetrahedron method with Blöchl corrections with 9051 nonequivalent tetrahedra.[59]

Figure 9a shows the corresponding PBE-SO band-structure computed along lines connecting high-symmetry points of the

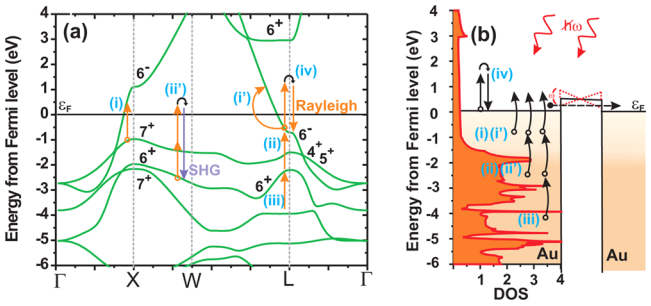

Figure 9. (a) Calculated PBE-SO band structure of Au using density functional theory. The zero energy is set at the Fermi level. The length of the arrows corresponds to the laser energy. The different transitions promoting electrons above the Fermi level are depicted. Processes (i) and (i′) represent interband and intraband transitions of electron located below ε_F near high symmetry point L or X, respectively. Nonlinear transitions are either resulting from a sequential absorption of two photons responsible for Au photoluminescence (ii) or a coherent absorption generating SHG (ii′). Process (iii) is involving a higher number of photons. (iv) represents Rayleigh scattering when there are no states to accommodate the optically excited electrons. (b) Calculated density of states (red curve) superposed with a drawing of the tunneling junction. The DOS is largely dominated by d-band electrons. The arrows represent the transition processes noted in (a) bringing low-lying electrons above ε_F that need to be taken into account in the photon-assisted transport.

first-Brillouin zone. The Fermi level is set at 0 eV. Electronic transitions resulting from the absorption of a photon are represented by arrows and are occurring around the high-symmetry X and L points of the Brillouin zone. The transition labeled (i) shows a direct absorption $X_{7^+\to 6^-}$. Indirect intraband excitations are also possible as in (i′) where the momentum mismatch for this nonvertical transition is brought by the high spatial frequency content of the electromagnetic field associated with the underlying Au nanostructure.[60] Processes (ii) and (ii′) depict nonlinear absorption mechanisms exciting d-band electrons above the Fermi level. These nonlinear absorptions

dx.doi.org/10.1021/nl404707t | Nano Lett. 2014, 14, 2330−2338

are rather efficient for gold nanostructures,[61−63] and especially optical gap antennas.[6,64] A strong nonlinear two-photon photoluminescence (TPL) response is typically observed resulting from a radiative interband recombination of an sp electron promoted above ε_F with a hole in the d-band[65,66] [process (ii)]. Another mechanism benefiting from the high density of d-bands is the SHG response depicted by (ii′)[67] and already introduced in Figure 3. Higher order excitations involving $n > 2$ photons are labeled (iii). These processes may include direct and indirect transitions. Finally, process (iv) depicts Rayleigh scattering occurring when electrons are excited above ε_F with momenta that do not coincide with an available state in the sp bands (the energy required for a direct intraband transitions to the L_{6^+} level is about 3 eV[54]).

While electronic transitions corresponding to instantaneous linear and nonlinear excitations (Rayleigh scattering and SHG) may not contribute to the photoassisted current, processes involving a real state like (i′), (ii), and (iii) supply electrons above the Fermi level that need to be considered to understand the optical dependence of the transport. Figure 9b shows the calculated total density of states (DOS) that include contributions from s, p, and d states (red curve). Superimposed on the DOS is a schematic drawing of the tunnel junction. While the state crossing the Fermi energy have sp-like properties, the DOS is largely dominated by d electrons below ε_F with a ratio to s states exceeding 2 orders of magnitude at the band edge.

Considering the above arguments, we hypothesize that optical excitations of d-band electrons to empty states close to the Fermi level are contributing to I_{phot} and are responsible for the nonlinearity of the junction displayed in Figure 8. The linear behavior for low laser intensity is consistent with the direct transition $X_{7^+\to 6^-}$ and indirect intraband transitions labeled (i′) in Figure 9. Because I_{phot} and I'' follow the same bias evolution (Figure 7), the higher order power dependence shown in the inset of Figure 8 suggests that optically excited low-lying electrons are contributing to the photocurrent [processes (ii) and (iii)]. The correlation between I_{phot} and I'' even in the nonlinear regime is rather surprising since eq 3 is valid only if the tunneling transmittance varies slowly on the voltage scale $\hbar\omega/e$,[24] which is clearly not the case when direct interband transitions are considered.[27] However, transitions (i′), (ii), or (iii) in Figure 9 are not direct coherent absorption processes mediated by virtual energy levels but are the results of a sequential absorption of two or more photons through short-lived metastable real states[65,66] and eq 3 remains valid.

We verify the role of promoted d-band electrons near the Fermi level by plotting the evolution with bias of the threshold value γ delimiting the linear to the nonlinear regime as defined in the inset of Figure 8. γ represents the laser intensity from which d-band electrons need to be taken into account in the photoconductance. The bias dependence of the γ threshold is reported in Figure 10. For $-0.45\ V < V_b < 0.3\ V$, γ is fairly constant at around $200 \pm 11\ kW/cm^2$. In this range of voltages, the rectenna operates in a direct tunneling regime ($eV_b < \phi^D$ and ϕ^S). The Fowler−Nordheim plot of the rectenna's electrical characteristic is reported in the inset of Figure 10. Here $\phi^D = 0.55$ eV and $\phi^S = 0.35$ eV. For larger V_b, we observe a sudden drop of the nonlinear threshold γ (~40%). This steplike decrease occurs at the onset of the transition voltages as indicated by the shaded areas in Figure 10. The figure indicates that the transport enters a nonlinear regime at lower input power if the operating bias is larger than the transition

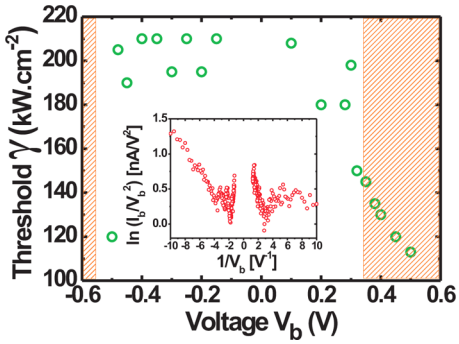

Figure 10. Evolution of the threshold γ defining the transition between the rectenna's linear to nonlinear regime as a function of bias V_b. The shaded areas show the voltage ranges in which the contacted gap antenna operates in field emission regime. The inset shows the Folwer−Nordheim representation of the junction's electrical characteristic. The two minima at −1.8 and 2.8 V^{-1} are the cross over biases from direct tunneling to field emission tunneling.

voltage. Under this Fowler−Nordheim field emission transport, the tunneling current become itself nonlinear with bias and more experiments are needed to distinguish between the different nonlinearities at play.

Conclusions. To conclude we show here that an optical gap antenna can act as an elementary nonlinear rectifier (rectenna) when irradiated by a femtosecond pulsed laser. We found that the rectenna's nonlinear characteristics can be controlled by the applied bias and emphasize the role of d-band electrons in the photon-assisted transport. We found that the rectenna's nonlinear characteristic can be controlled by the applied bias. Although the rectenna geometry is relatively simple, the optical gap and the electrical rectifying gap are self-aligned at the nanometer scale. Enhancement of the photocurrent yield can be achieved by controlling the intrinsic feed characteristics of these two overlapping functional gaps. Engineering the barrier height and the geometrical asymmetry of the facing edges will increase substantially the classical responsivity S of the rectenna.[25] Deploying a resonant plasmonic feedgap will improve the interaction cross-section of the rectenna with the incoming photons[23,68] and will provide an enhancement of the localized electromagnetic field.[10] These combined effects will contribute to increase the efficiency of the rectenna, paving thus the deployment of these unique interfacing devices in an optoelectronic information processing platform. Finally, we note that Figure 3 or Figure 8 shows time-averaged photocurrent maps and laser intensity dependencies. Because the laser produces 180 fs short pulses at a repetition rate of 80 MHz, the measured current at the terminals is constituted of a rectified electron packets bunched on a similar time scale. By using pulse-picking technique, femtosecond electron pulses can thus be delivered on-demand in a circuitry. This simple optical rectenna could therefore be implemented as a wired ultrafast electron source for studying temporal dynamics of nanoscale electronic devices and serve as an extremely local source of terahertz radiation.

AUTHOR INFORMATION

Corresponding Author

*E-mail: alexandre.bouhelier@u-bourgogne.fr.

Present Addresses

(A.S.) Institut Interdisciplinaire d'Innovation Technologique (3IT), Laboratoire Nanotechnologies Nanosystèmes (LN2)-

CNRS UMI-3463, Université de Sherbrooke, 3000 Boulevard Université Sherbrooke, J1K OA5, Québec, Canada.
(J.B.) ICFO, The Institute of Photonic Sciences, Av. Carl Friedrich Gauss, 3, 08860 Castelldefels (Barcelona) Spain.

Notes

The authors declare no competing financial interest.

■ ACKNOWLEDGMENTS

A.B. thanks valuable discussions with L. Novotny, A. G. Borisov, P. Bharadwaj, M. Frimmer, and A. Dereux. The research leading to these results has received funding from the European Research Council under the European Community's Seventh Framework Program FP7/2007-2013 Grant Agreement 306772. This project is in cooperation with the Labex ACTION program (contract ANR-11-LABX-01-01). A.S. acknowledges a scholarship from Région de Bourgogne under the PARI initiative. V. M. acknowledges support from the State of New York though its NYStar program.

■ REFERENCES

(1) Schuller, J. A.; Barnard, E. S.; Cai, W.; Jun, Y. C.; White, J. S.; Brongersma, M. L. *Nat. Mater.* **2010**, *9*, 193−204.
(2) Halas, N. J.; Lal, S.; Chang, W.-S.; Link, S.; Nordlander, P. *Chem. Rev.* **2011**, *111*, 3913−3961.
(3) Schwartzberg, A. M.; Grant, C. D.; Wolcott, A.; Talley, C. E.; Huser, T. R.; Bogomolni, R.; Zhang, J. Z. *J. Phys. Chem. B* **2004**, *108*, 19191−19197.
(4) Ahmed, A.; Gordon, R. *Nano Lett.* **2012**, *12*, 2625−2630.
(5) Danckwerts, M.; Novotny, L. *Phys. Rev. Lett.* **2007**, *98*, 026104.
(6) Ghenuche, P.; Cherukulappurath, S.; Taminiau, T. H.; F. van Hulst, N.; Quidant, R. *Phys. Rev. Lett.* **2008**, *101*, 116805.
(7) Slablab, A.; Xuan, L. L.; Zielinski, M.; de Wilde, Y.; Jacques, V.; Chauvat, D.; Roch, J.-F. *Opt. Express* **2012**, *20*, 220−227.
(8) Berthelot, J.; Bachelier, G.; Song, M.; Rai, P.; Colas des Francs, G.; Dereux, A.; Bouhelier, A. *Opt. Express* **2012**, *20*, 10498−10508.
(9) Romero, I.; Aizpurua, J.; Bryant, G. W.; García de Abajo, F. J. *Opt. Express* **2006**, *14*, 9988.
(10) García-Martín, A.; Ward, D. R.; Natelson, D.; Cuevas, J. C. *Phys. Rev. B* **2011**, *83*, 193404.
(11) Kern, J.; Gromann, S.; Tarakina, N. V.; Häckel, T.; Emmerling, M.; Kamp, M.; Huang, J.-S.; Biagioni, P.; Prangsma, J. C.; Hecht, B. *Nano Lett.* **2012**, *12*, 5504−5509.
(12) Esteban, R.; Borisov, A. G.; Nordlander, P.; Aizpurua, J. *Nat. Commun.* **2012**, *3*, 825.
(13) Savage, K. J.; Hawkeye, M. M.; Esteban, R.; Borisov, A. G.; Aizpurua, J.; Baumberg, J. J. *Nature (London)* **2012**, *491*, 574.
(14) Scholl, J. A.; García-Etxarri, A.; Koh, A. L.; Dionne, J. A. *Nano Lett.* **2013**, *13*, 564−569.
(15) Wu, L.; Duan, H.; Bai, P.; Bosman, M.; Yang, J. K. W.; Li, E. *ACS Nano* **2013**, *7*, 707−716.
(16) Novotny, L.; Van Hulst, N. F. *Nat. Photonics* **2011**, *5*, 83−90.
(17) Knight, M. W.; Sobhani, H.; Nordlander, P.; Halas, N. J. *Science* **2011**, *332*, 702−704.
(18) Siu, D.; Jain, R. K.; Gustafson, T. K. *Appl. Phys. Lett.* **1976**, *28*, 407.
(19) Miskovsky, N. M.; Cutler, P. H.; Mayer, A.; Weiss, B. L.; Willis, B.; Sullivan, T. E.; Lerner, P. B. *J. Nanotechnol.* **2012**, *2012*, 512379.
(20) Marinica, D.; Kazansky, A.; Nordlander, P.; Aizpurua, J.; Borisov, A. G. *Nano Lett.* **2012**, *12*, 1333−1339.
(21) Dombi, P.; Hörl, A.; Rácz, P.; Márton, I.; Trügler, A.; Krenn, J. R.; Hohenester, U. *Nano Lett.* **2013**, *13*, 674−678.
(22) Ward, D. R.; Hüser, F.; Pauly, F.; Cuevas, J. C.; Natelson, D. *Nat. Nanotechnol.* **2010**, *5*, 732−736.
(23) Prangsma, J. C.; Kern, J.; Knapp, A. G.; Grossmann, S.; Emmerling, M.; Kamp, M.; Hecht, B. *Nano Lett.* **2012**, *12*, 3915−3919.
(24) Tucker, J. *IEEE J. Quantum Electron.* **1979**, *15*, 1234.
(25) Mayer, A.; Chung, M. S.; Lerner, P. B.; Weiss, B. L.; Miskovsky, N. M.; Cutler, P. H. *J. Vac. Sci. Technol., B* **2011**, *29*, 041802.
(26) Arielly, R.; Ofarim, A.; Noy, G.; Selzer, Y. *Nano Lett.* **2011**, *11*, 2968−2972.
(27) Viljas, J. K.; Cuevas, J. C. *Phys. Rev. B* **2007**, *75*, 075406.
(28) Park, H.; Lim, A. K. L.; Park, J.; Alivisato, A. P.; McEuen, P. L. *Appl. Phys. Lett.* **1999**, *75*, 301.
(29) Mangin, A.; Anthore, A.; Della Rocca, M. L.; Boulat, E.; Lafarge, P. *Phys. Rev. B* **2009**, *80*, 235432.
(30) Stahlmecke, B.; Meyer zu Heringdorf, F.-J.; Chelaru, L. I.; Horn-von Hoegen, M.; Dumpich, G. *Appl. Phys. Lett.* **2006**, *88*, 053122.
(31) Steinmann, P.; Weaver, J. M. R. *J. Vac Sci. Technol., B* **2004**, *22*, 3178−3181.
(32) Beebe, J. M.; Kim, B.; Gadzuk, J. W.; Frisbie, D. C.; Kushmerick, J. G. *Phys. Rev. Lett.* **2006**, *97*, 026801.
(33) Trouwborst, M. L.; Martin, C. A.; Smit, R. H. M.; Gudon, C. M.; Baart, T. A.; van der Molen, S. J.; van Ruitenbeek, J. M. *Nano Lett.* **2011**, *11*, 614−617.
(34) Wu, K.; Bai, M.; Sanvito, S.; Hou, S. *Nanotechnology* **2013**, *24*, 025203.
(35) Taychatanapat, T.; Bolotin, K. I.; Kuemmeth, F.; Ralph, D. C. *Nano Lett.* **2007**, *7*, 652−656.
(36) Dey, S.; Mirell, D.; Perez, A. R.; Lee, J.; Apkarian, V. A. *J. Chem. Phys.* **2013**, *138*, 154202.
(37) Mayer, A.; Chung, M. S.; Weiss, B. L.; Miskovsky, N. M.; Cutler, P. H. *Phys. Rev. B* **2008**, *78*, 205404.
(38) Grafström, S. *J. Appl. Phys.* **2002**, *91*, 1717−1750.
(39) Gamaly, E. *Femtosecond Laser-Matter Interaction: Theory, Experiments and Applications*; Pan Stanford Publishing Pte. Ltd: Singapore, 2011.
(40) Kopp, B.; Yi, Z.; Benner, D.; Xie, F. Q.; Obermair, C.; Schimmel, T.; Boneberg, J.; Leiderer, P.; Scheer, E. *Beilstein J. Nanotechnol.* **2012**, *3*, 703−711.
(41) Guhr, D. C.; Rettinger, D.; Boneberg, J.; Erbe, A.; Leiderer, P.; Scheer, E. *Phys. Rev. Lett.* **2007**, *99*, 086801.
(42) Carlson, M. T.; Green, A. J.; Khan, A.; Richardson, H. H. *J. Phys. Chem. C* **2012**, *116*, 8798−8803.
(43) Herzog, J. B.; Knight, M. W.; Natelson, D. *Nano Letters* **2014**, *14*, 499−503.
(44) Shi, S.-F.; Xu, X.; Ralph, D. C.; McEuen, P. L. *Nano Lett.* **2011**, *11*, 1814−1818.
(45) Yajadda, M. M. A.; Muller, K.-H.; Farrant, D. I.; Ostrikov, K. *Appl. Phys. Lett.* **2012**, *100*, 211105.
(46) Thon, A.; Merschdorf, M.; Pfeiffer, W.; Klamroth, T.; Saalfrank, P.; Diesing, D. *Appl. Phys. A: Mater. Sci. Process.* **2004**, *78*, 189−199.
(47) Schenk, M.; Krüger, M.; Hommelhoff, P. *Phys. Rev. Lett.* **2010**, *105*, 257601.
(48) Wang, F.; Melosh, N. A. *Nat. Commun.* **2013**, *4*, 1711.
(49) Chalabi, H.; Schoen, D.; Brongersma, M. L. *Nano Lett.* **2014**, *14*, 1374−1380.
(50) Govorov, A. O.; Zhang, H.; Gunko, Y. K. *J. Phys. Chem. C* **2013**, *117*, 16616−16631.
(51) Govorrov, A. O.; Zhang, H.; Demir, H. V.; Gun'ko, Y. K. Photogeneration of hot plasmonic electrons with metal nano crystals: Quantum description and potential applications. *Nano Today* 2014, in press; http://dx.doi.org/10.1016/j.nantod.2014.02.006.
(52) Bormann, R.; Gulde, M.; Weismann, A.; Yalunin, S.; Ropers, C. *Phys. Rev. Lett.* **2010**, *105*, 147601.
(53) Jaklevic, R. C.; Lambe, J. *Phys. Rev. B* **1975**, *12*, 4146−4160.
(54) Rangel, T.; Kecik, D.; Trevisanutto, P. E.; Rignanese, G.-M.; Van Swygenhoven, H.; Olevano, V. *Phys. Rev. B* **2012**, *86*, 125125.
(55) Perdew, J. P.; Burke, K.; Ernzerhof, M. *Phys. Rev. Lett.* **1996**, *77*, 3865−3868.
(56) Romaniello, P.; de Boeij, P. L. *J. Chem. Phys.* **2005**, *122*, 044104.
(57) Kresse, G.; Hafner, J. *Phys. Rev. B* **1993**, *47*, 558−561.
(58) Kresse, G.; Joubert, D. *Phys. Rev. B* **1999**, *59*, 1758−1775.
(59) Blöchl, P. E.; Jepsen, O.; Andersen, O. K. *Phys. Rev. B* **1994**, *49*, 16223−16233.

(60) Beversluis, M. R.; Bouhelier, A.; Novotny, L. *Phys. Rev. B* **2003**, *68*, 115433.
(61) Chen, C. K.; Heinz, T. F.; Ricard, D.; Shen, Y. R. *Phys. Rev. B* **1983**, *27*, 1965.
(62) Bouhelier, A.; Beversluis, M.; Novotny, L. *Appl. Phys. Lett.* **2003**, *82*, 4596.
(63) Dulkeith, E.; Niedereichholz, T.; Klar, T. A.; Feldmann, J.; von Plessen, G.; Gittins, D. I.; Mayya, K. S.; Caruso, F. *Phys. Rev. B* **70**, *70*, 205424.
(64) Palomba, S.; Danckwerts, M.; Novotny, L. *J. Opt. A: Pure Appl. Opt.* **2009**, *11*, 114030.
(65) Imura, K.; Nagahara, T.; Okamoto, H. *J. Phys. Chem. B* **2005**, *109*, 13214−13220.
(66) Biagioni, P.; Celebrano, M.; Savoini, M.; Grancini, G.; Brida, D.; Mátéfi-Tempfli, S.; Mátéfi-Tempfli, M.; Duò, L.; Hecht, B.; Cerullo, G.; Finazzi, M. *Phys. Rev. B* **2009**, *80*, 045411.
(67) Luce, T.; Hbner, W.; Bennemann, K. *Z. Phys. B: Condens. Matter* **1997**, *102*, 223−232.
(68) Mayer, A.; Cutler, P. H. *J. Phys.: Condens. Matter* **2009**, *21*, 395304.